



# OPEN Effect of grain dissolution on sloping ground

Minsu Cha<sup>1✉</sup> & J. Carlos Santamarina<sup>2</sup>

The static and dynamic stability of natural or constructed slopes can be affected by dissolution or dissolution-like phenomena. Their underlying mechanisms, however, remain unclear. New experimental results and discrete element simulations provide particle-level and macroscale information on the consequences of mineral dissolution on slope behavior. At the microscale, load-carrying grain arches develop around dissolving particles, the porosity increases, and contact force chains evolve to form a honeycomb topology. At the macroscale, while vertical settlements are the prevailing deformation pattern, lateral granular movements that create mass wasting are prominent in sloping ground, even under the quasi-static granular loss. Horizontal grain displacement is maximum at the surface and decreases linearly with the distance from the slope surface to become zero at the bottom boundaries, much like vertical granular displacement along the depth. Sediments with smaller friction angles and steeper slopes experience greater displacement, both vertically and horizontally. Slopes become flatter after dissolution, with the reduction in slope angle directly related to the loss in ground elevation,  $\Delta H/H_0$ . Yet, because of the porous fabric that results from dissolution, vertical shortening is less than the upper bound, estimated from the loss in the solid mass fraction,  $\Delta H/H_0 \approx SF$ . Under water-saturated conditions, the post-dissolution fabric may lead to sudden undrained shear and slope slide.

Dissolution and reprecipitation are prevalent and persistent diagenetic processes. The time scale for chemical processes is typically quite long and the “inert assumption of soils” applies to many engineering applications. However, dissolution and precipitation can also take place within relatively short time scales in advective regimes such as infiltration-induced carbonate dissolution and when systems are taken far from equilibrium in young systems such as dam foundations, mine tailings, fly ash, volcanic ash, and CO<sub>2</sub> injection<sup>1–13</sup>.

Waste is particularly vulnerable to dissolution and degradation because its components are suddenly exposed to new environmental conditions outside equilibrium. Heavy metals and acid drainage from mine tailings and fly ash ponds are early signs of ongoing dissolution processes<sup>14,15</sup>. Likewise, some components in fly ash, including CaO and CaSO<sub>4</sub>, are highly soluble<sup>16,17</sup>. The dissolution of coal ash grains contributes to instability and collapse<sup>18</sup>; on the other hand, new minerals such as zeolite and phillipsite can precipitate<sup>19,20</sup>. Dissolution and reprecipitation lead to porous yet cemented sediments that are brittle and contractive and are vulnerable to liquefaction once perturbed. The potential for slope instability due to solid phase loss could affect waste disposal (including organic waste, mine tailings, and coal ash).

Many natural ground movements involve some form of solid phase loss, albeit not necessarily mineral dissolution. Repetitive diurnal or seasonal freeze–thaw that involves the thawing of ice needles and segregated ice cause a downslope ratcheting movement, termed solifluction<sup>21–24</sup>. The failure of the Carsington Dam occurred along a pre-existing solifluction shear plane within the foundation layer<sup>25,26</sup>. In recent decades, diminishing permafrost in high mountains and polar regions has increasingly caused landslides<sup>27–30</sup> and contributed to the destabilization of rock structures<sup>31,32</sup>.

Similarly, gas hydrate dissociation is one of the major causes of large-scale submarine landslides<sup>33–37</sup>, seen in the Storegga Slide<sup>38,39</sup> and the Trænadjupet Slide<sup>40,41</sup>. Hydrate dissociation not only involves solid mass loss but also accompanies gas generation and expansion, which results in marked excess pore pressure generation and effective stress loss<sup>33,42</sup>. Gas hydrate dissociation can be naturally triggered by sea-level fluctuations<sup>43</sup> and rising ocean temperatures<sup>44</sup>, and is unavoidable in the vicinity of platform foundations<sup>34,45</sup>. In addition, dissolution may be purposely caused for gas production<sup>46</sup>.

As described above, many studies have attributed slope movement in the field to dissolution or dissolution-like phenomena. To date, however, no study has closely examined the effects of the mechanisms of dissolution on the behavior of sloping ground. Therefore, the purpose of this research is to explore the stability and deformation

<sup>1</sup>Department of Civil Engineering, College of Ocean Sciences, Jeju National University, Jeju-Si, Jeju Special Self-Governing Province 63243, Republic of Korea. <sup>2</sup>Earth Science and Engineering, King Abdullah University of Science and Technology (KAUST), Thuwal 23955-6900, Saudi Arabia. ✉email: mcha@office.jejunu.ac.kr

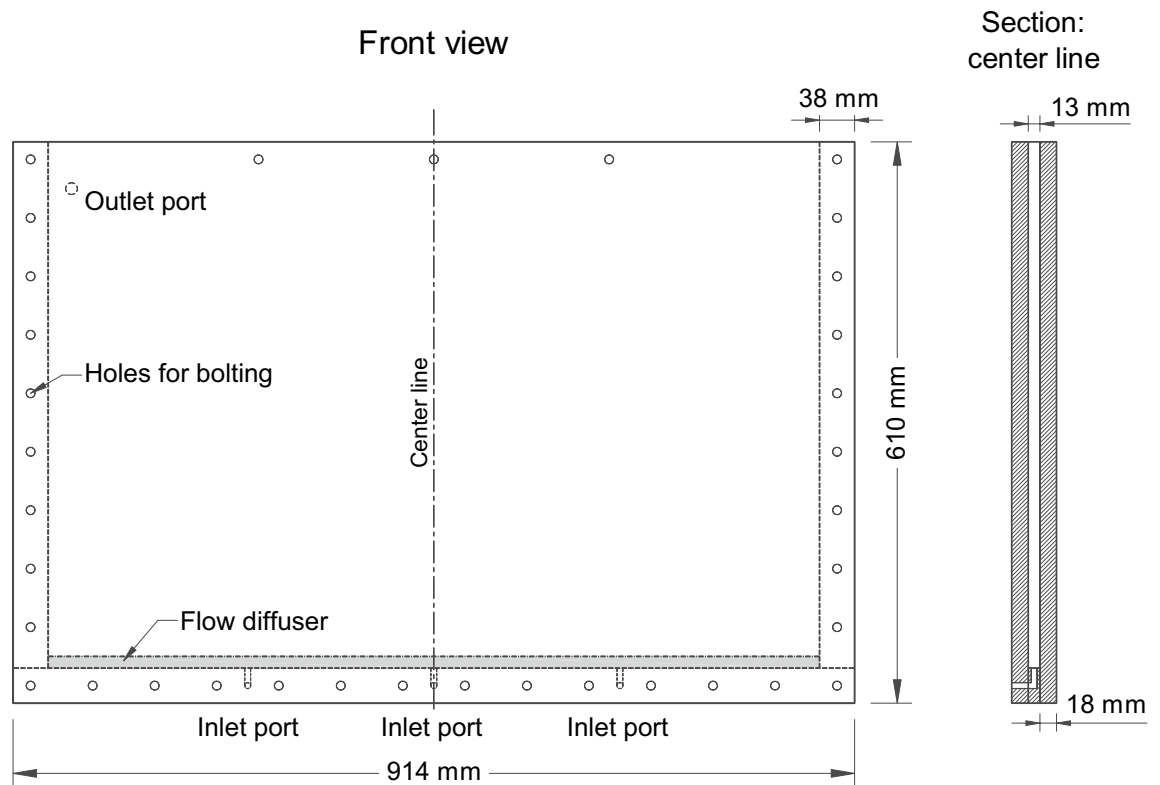


**Figure 1.** Transparent two-dimensional tank used to explore the effects of dissolution on slope stability.

of sloping ground due to solid phase loss such as mineral dissolution. In particular, we aim to understand mass wasting characteristics during dissolution in dry, drained conditions using micro- and macro-scale information gathered from discrete element simulations and any emergent behavior when dissolution occurs underwater using a laboratory model test.

The research approach combines a high-caliber 1 g laboratory experiment and a series of discrete element simulations. Note that the two approaches are not designed to match the conditions of each method but to complement and harness their respective advantages. For example, the experiment uses saturated specimens while the DEM employs dry specimens.

### Experimental study

We designed and conducted a 1 g laboratory experiment to explore the consequences of dissolution in slopes under water-saturated conditions, which is a common field condition during dissolution.

**Device and specimen.** The experimental study used a thin tank made of two parallel, transparent acrylic plates (width 18 mm, separated by a 13 mm gap; Fig. 1). The thick acrylic walls were 914 mm × 610 mm and firmly fixed to spacers at the four edges of the tank to minimize the horizontal deflection of the walls, which results from the sediment weight. Inlet ports at the bottom were covered with a flow diffuser that ran along the full base beneath the sediment, which enabled a true 1D flow and promoted uniform dissolution (Fig. 1).

The results presented herein correspond to a sediment made of 90% sand (insoluble grains:  $D_{50} = 0.16$  mm,  $G_s = 2.65$ , subround, poorly graded, a global friction angle of  $38^\circ$ ) and 10% salt (soluble grains:  $D_{50} = 0.3$  mm,  $G_s = 2.165$ , cubical, poorly graded) by weight, creating a mixture with a soluble fraction (SF) of 10%. Sand and salt were dry-mixed and then pluviated into the tank, forming the slope, with an initial angle of  $30^\circ$ . As the specific gravities of insoluble ( $G_U = 2.65$ ) and dissolvable grains ( $G_D = 2.165$ ) differ, we used their weighted average to calculate the initial global porosity:

$$n = 1 - \frac{\rho_{dry} (1 - m)G_D + mG_U}{\rho_w G_U G_D} \quad (1)$$

where  $m$  = mass fraction of dissolvable grains; and densities  $\rho_w$  and  $\rho_{dry}$  correspond to water and the dry mixture, respectively. The initial porosity measurement  $n_0$  is 0.412 (medium loose).

**Test procedure and conditions.** The model was slowly flooded with a saturated NaCl brine solution permeated from the bottom (duration: 5 h); brine prevented the dissolution of the salt mixed in with the sand. The gradual dissolution was controlled by progressively lowering the salt concentration in the permeated fluid (duration: 3 days). These slow and progressive changes in salt concentration over the long period ensured all

soluble particles decreased in size at the same time (a “homogeneous dissolution” as in Cha and Santamarina<sup>47</sup>). The low reaction rate (low Damkohler number) guaranteed uniform dissolution and avoided preferential dissolution modes such as localized dissolution and face dissolution initiated from the inlet boundary. In addition, a very low hydraulic gradient ( $i < 0.1$ ) was maintained for the saturation and flow so that it created negligible uplift pressure on the sediment particles. A camera recorded the slope deformation by high-resolution time-lapse imaging with a five-minute time interval. The experimental setup was isolated on a heavy, vibration-free table during dissolution.

While it is impossible to simulate the time scale of dissolution in the field, we ensured that the laboratory dissolution was very gradual, as demonstrated by the long and uniform dissolution. Consequently, the system behaved quasi-statically.

Previous research has used the inertial number ( $I$ ) to quantify the dynamic effects in particulate discrete element simulations<sup>48</sup> and experimental analysis<sup>49</sup>. The calculated inertial number was  $\sim 10^{-8}$  for the particles on the surface, which is well within quasi-static criteria ( $I < 10^{-3}$ ).

**Experimental results.** Digital image correlations failed to provide adequate displacement fields—from the start to the end—due to a lack of contrast in the sediment. Instead, we manually traced displacements of clearly visible and persistent impurities detectable in high-resolution images. The results in Fig. 2a show the displacement vectors from the beginning to the end of dissolution, which demonstrate that vertical displacements prevail, the magnitude of vertical displacements increases almost linearly with elevation, and horizontal displacements become increasingly prominent towards the slope surface. An areal analysis of the specimen shows that the total volume decreases by 7.5%, with the dissolved fraction of 12% by solid volume (10% by weight), which provides the calculation of the increase in porosity from the initial porosity  $n_0 = 0.412$  to final porosity  $n_f = 0.440$ .

Notably, we detected a sudden displacement when all the recorded images were played as a movie sequence. Figure 2b presents the two consecutive images that highlight this sudden displacement. Digital image correlation did capture the sudden movement between these consecutive images; see Fig. S1 in the Supplemental Data. The displacement vectors defined a shallow failure surface. The maximum possible duration for this local failure is the time interval between photographs  $\Delta t = 5$  min (although the fact that the localization is solely contained within the two consecutive images indicates the actual duration could be arbitrarily much shorter). Given a drainage length similar to the slide depth,  $d = 10$  cm, the coefficient of consolidation for drained conditions should be higher than  $c_v > d^2/\Delta t = 0.3$  cm<sup>2</sup>/s, which corresponds to fine sands. These results suggest that this local failure took place under undrained conditions.

A possible mechanism leading to the slide could involve the following sequence of events, as also illustrated in Fig. 3. Granular dissolution results in increased porosity, as shown in this experiment and other work, and the sediment becomes contractive<sup>47</sup>. At the same time, internal stress states approach the Coulomb failure condition, i.e.,  $K_a$ <sup>50</sup>. Therefore, the active failure condition initiated the structural collapse of the porous granular skeleton. This sudden collapse combined with the highly contractive tendency of the post-dissolution sediments<sup>47</sup> can lead to the temporal generation of excess pore pressure, as described in the above paragraph, and a decrease in the effective stress, which lowered shear strength and resulted in the slope failure/slide.

We used low-friction, scratch-free acrylic plates for the lateral walls. Nevertheless, the boundaries may create friction between the particles and lateral walls and could lessen granular movement at the boundaries to some degree. First, during dissolution, friction may reduce settlement and then once shear localization initiates, it will potentially reduce the amount of movement. Indeed, our shear slide occurred over a short distance. The fact that the localization occurred in spite of the boundary friction may indicate a more substantial slide in a 3D experiment with a large lateral dimension.

## Discrete element simulations

The consequences of dissolution on sloping ground were studied further using two-dimensional (2D) discrete element method (DEM) simulations via Particle Flow Code (PFC) 2D by Itasca. Unlike the experiments, the DEM simulations were dry or drained (no fluid module). These conditions still have relevance in dissolution under unsaturated conditions (e.g., by repeated rainwater infiltrations)<sup>51,52</sup>, and solifluction in partially saturated ground, or even saturated slopes of coarse-grained sediments that do not experience localization during dissolution. While not emulating the exact conditions, the simulations and experiments gather complementary information.

**Simulation environment and geometry.** Table 1 shows the basic simulation environment and material properties. The 2D simulations used the linear contact model with normal stiffness  $k_n = 10^8$  N/m and shear stiffness  $k_s = 10^8$  N/m. As noted above, conditions were dry/drainage, and there was no side friction against the front or back walls. Additionally, there is no friction between the sediment and the vertical lateral walls, which allowed the 1D settlement of the level ground portion subjected to uniform dissolution. The friction coefficient between the sediment and the lower boundary (non-dissolving base material) was 0.5 (Fig. 4f). The stiffnesses of the contact model and the inter-particle friction were selected based on the literature and the software manual<sup>53–56</sup>. The sediment consisted of disks that were placed at random locations within the model geometry and allowed to grow to their final target size (i.e., uniform size distribution with  $R_{\min} = 0.4$  mm and  $R_{\max} = 0.6$  mm).

Grain angularity and interlocking, which imply rotational resistance, can be numerically implemented by imposing rolling resistance<sup>57–60</sup> or by the introduction of non-spherical particles and granular clusters<sup>61–64</sup>. Hindered particle rotation is a computationally efficient approach that accounts for grain angularity<sup>65,66</sup>. Numerical results are physically inconsistent when all particles have hindered rotation; in this study, we hindered the rotation of a preselected percentage of randomly located particles, that is, hinder rotation (HR) of 0%, 40%, and 80%.

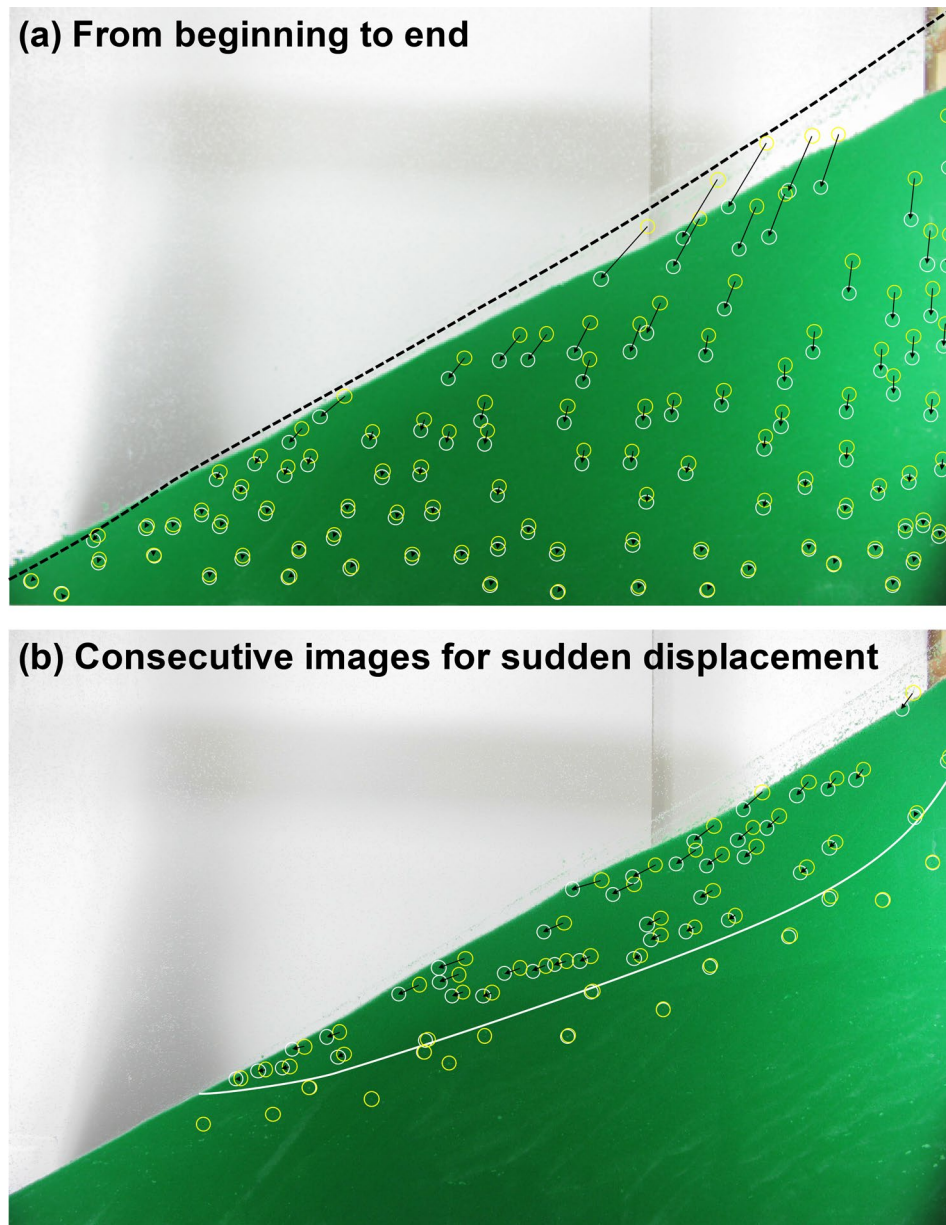


**Figure 2.** Experimental results. Displacement vectors at visually recognizable points: **(a)** From the beginning to the end of dissolution. Note: The dotted line indicates the original slope surface; **(b)** Sudden shear failure observed during a 5-min photo-interval. This test corresponds to a specimen mixed with a mass fraction SF = 10% of dissolvable particles. Note: Displacement vectors are shown at the same scale in both **(a)** and **(b)**.

to simulate different levels of granular interlocking or macroscopic friction<sup>67</sup>. For a discussion and calibration of this approach with the experimental results of Shin and Santamarina<sup>50</sup>, see Cha and Santamarina<sup>47</sup>. Although this approach did mimic the macroscopic trends and global-scale micromechanical parameters, it created more unnatural behaviors than those from computationally expensive techniques that use realistic particle shapes; in particular, we observed excessive, localized dilation around rotationally hindered particles.

Simulations used three initial slope angles:  $\beta = 20^\circ$ ,  $30^\circ$ , and  $40^\circ$  (Fig. 4). The numerically measured angle of repose,  $\Phi_r$ , increased with the percentage of particles with hindered rotation:  $\Phi_r = 22^\circ$  for HR = 0%,  $\Phi_r = 35^\circ$  for HR = 40%, and  $\Phi_r = 48^\circ$  for HR = 80%<sup>67</sup>. Therefore, only the slope with  $\beta_o = 20^\circ$  was stable when HR = 0%; the slopes with  $\beta_o = 20^\circ$  and  $30^\circ$  were stable for HR = 40%; and the three slopes with  $\beta_o = 20^\circ$ ,  $30^\circ$ , and  $40^\circ$  were stable when HR = 80%. The specimen dimensions for the  $\beta = 20^\circ$  cases are a base length of 284 mm and height of 72 mm.

**Dissolution simulation.** Soluble particles were randomly selected and, thus, homogeneously distributed in the preformed granular packing (soluble particles shown in red; Fig. 4). The mass fraction of soluble particles (SF) accounted for SF = 25% of all particles. Note soluble fractions in a given sediment that contains water-soluble minerals such as carbonate and evaporite can vary greatly<sup>68,69</sup>.

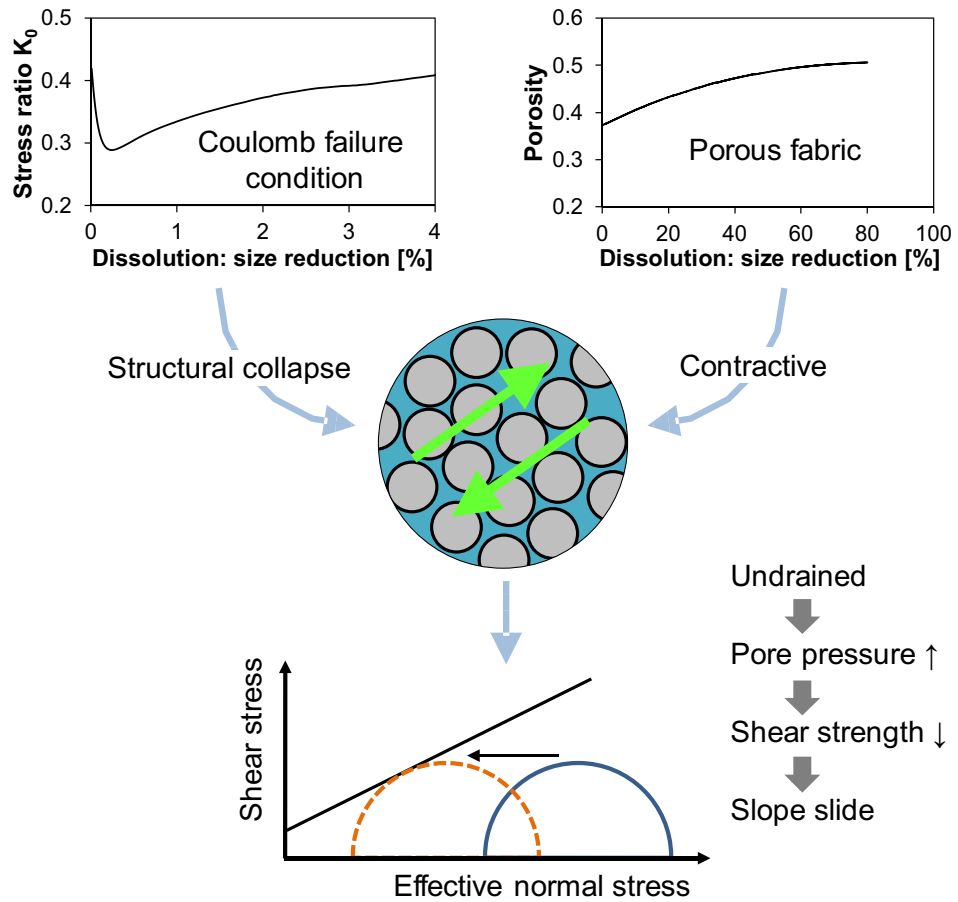


**Figure 3.** Sequence of conditions leading to the slide. The stress ratio  $K_0$  and porosity are from the three-dimensional discrete element simulations in Cha and Santamarina<sup>47</sup>.

	Properties	Values
Particles (disks)	Particle size distribution	Uniform size distribution ( $R_{min} = 0.4$ mm, $R_{max} = 0.6$ mm)
	Number of particles	10,567
	Mass density of particles	2650 kg/m <sup>3</sup>
	Linear contact model	Normal stiffness $k_n = 10^8$ N/m Shear stiffness $k_s = 10^8$ N/m
	Inter-particle friction	0.5
	Fraction of soluble particles	25%
	Hindered rotation, HR	0%, 40% and 80%
Boundary conditions	Initial slope angle	20°, 30° and 40°
	Particle-to-wall friction	0.5 for the base 0 for the wall

**Table 1.** Two-dimensional discrete element simulation environment.

Smooth and gradual size reduction prevented numerical instability and dynamic effects. The dissolution of soluble particles was performed by gradually and simultaneously reducing the radius of all the soluble particles at the same rate<sup>70</sup>. In particular, the gradual size reduction involved numerous steps of minute size reduction (specifically, a radius reduction of 1/50,000 times the initial radius in each step), with each step followed by a full equilibrium stage<sup>47,71</sup>. In addition, the ratio of the mean unbalanced force to the mean contact force was always smaller than 0.001, which ensured stable conditions throughout the dissolution process.

The inertial number  $I$  is the ratio between the time for a given displacement when accelerated by the stress-dependent skeletal forces  $\sigma'd^2$  and the time for the same displacement given an imposed strain rate  $\dot{\gamma}$ <sup>48,72</sup>:

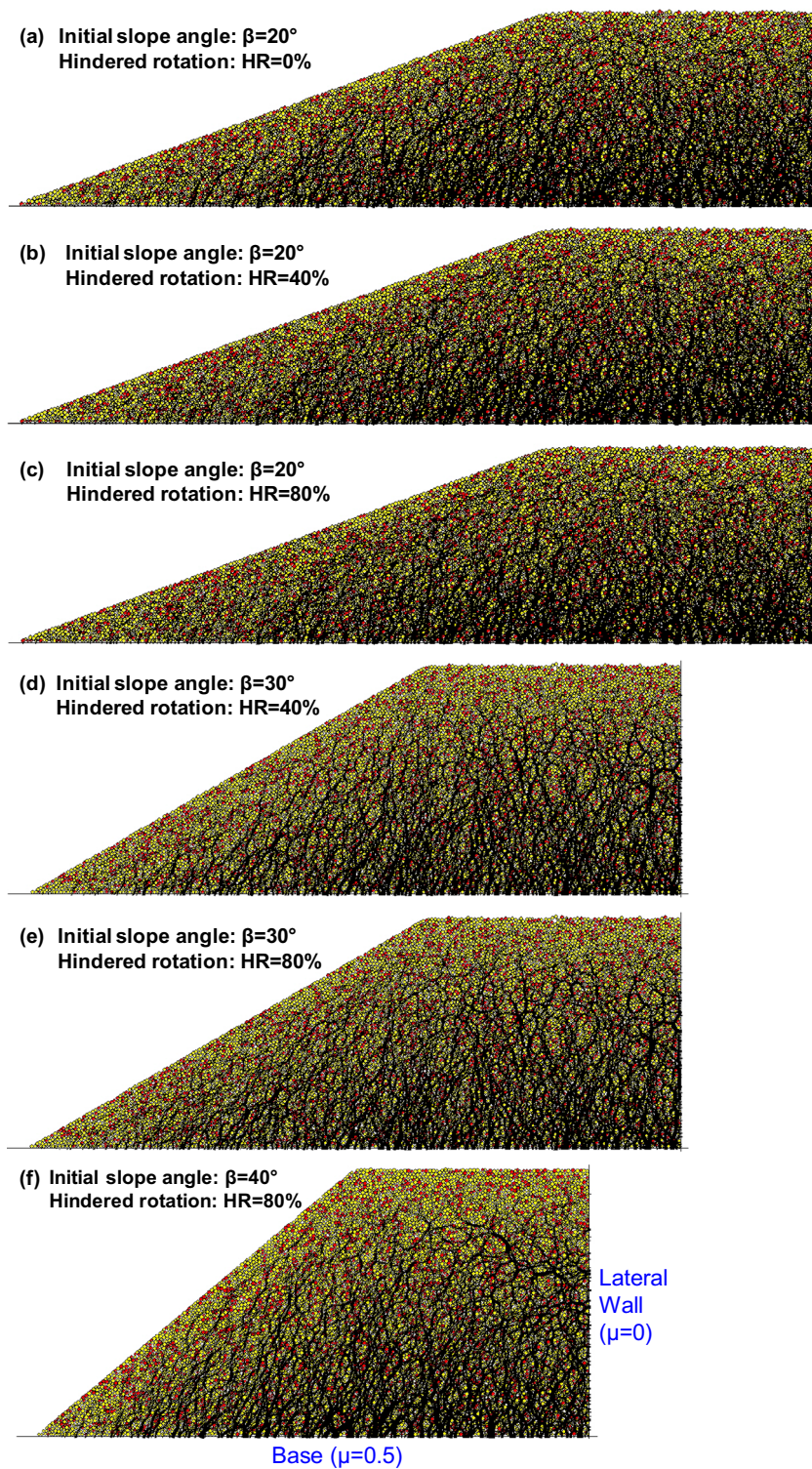


**Figure 4.** Specimen preparation and contact force chains before dissolution – All cases are shown at the same force scale. Soluble particles are shown in red (SF = 25%). Note the number of particles are the same for all simulations (10,567).

$$I = \frac{\dot{\gamma}d}{\sqrt{\sigma'/\rho}} \quad (2)$$

For particles of diameter  $d = 1$  mm, grain density  $\rho = 2650$  kg/m<sup>3</sup>, average effective stress  $\sigma' = 0.02$  kPa of surface particles (the most critical case), and particle shrinking rate  $\dot{\gamma} = 0.017$ /s, the computed inertial number  $I \approx 2 \times 10^{-4}$  is within the quasi-static criterion  $I < 10^{-3}$  for strain rate independent frictional resistance. For the global movement, applying a slope movement rate  $\dot{\gamma} = 0.004$ /s and an effective stress 0.6 kPa (at mid depth), the calculated  $I$  is  $8 \times 10^{-6}$ .

Macroscale parameters stabilized when the sizes of dissolvable particles decreased to 10% of the initial sizes. We ended our simulations when the particle sizes reduced to 1% of their initial sizes. The time step was set to  $\Delta t = 0.6\sqrt{m/K}$ , where  $m$  is the particle mass and  $K$  the particle stiffness; the time step changed as the grain mass  $m$  diminished during the simulations. The physical time for the dissolution simulations was about 2 min while the computation time exceeded several weeks. Observations from the simulation results follow.

**Contact force and internal fabric.** Contact forces form characteristic “chains” in granular materials. Force chains are evenly distributed before dissolution in our simulations and have a preferentially vertical orientation in agreement with the typical stress ratio  $K_0 \approx 0.45$  under normal compaction, yet the principal direction of force chains deviate from the vertical near the slope (Fig. 4). Figure 5 shows that higher stress anisotropy exists in the sloping ground (from the surface to the base) in its initial condition. The larger slope angle creates higher values of maximum shear stresses divided by the mean normal stresses.

Force redistribution starts after the dissolvable particles begin to contract; forces initially carried by dissolvable grains transfer to neighboring grains during dissolution (see the video—Supplementary Data). Preponderant interparticle force chains form arches around developing voids in a honeycomb-like fabric (Fig. 6). The honeycomb-shaped network of force chains was more prominent in sediments with more granular interlocking, that is, packings with a higher fraction of rotationally hindered particles, HR (Fig. 6). The coordination number decreased for all cases: from an initial value of 3.62 (all cases), to 2.38 (no hindered rotation), 2.28 (HR = 40%) and 2.09 (HR = 80%) at the end of dissolution. The state of stress became more stable after dissolution, especially for the mid slope.

**Porosity and pores.** The final overall porosity increased in all cases: from an initial value of  $n_0 = 0.155$  (Dense; all cases), to  $n = 0.205$  (no hindered rotation),  $n = 0.216$  (HR = 40%) and  $n = 0.243$  (HR = 80%) at the end of dissolution, similar to the experimental results. Complementary results of the evolution of porosity and other parameters during dissolution for three-dimensional simulations and experiments can be found in Cha and Santamarina<sup>73</sup> and Cha and Santamarina<sup>47</sup>.

Careful inspection of the images in Fig. 6 reveals large remnant voids located next to major contact force chains after dissolution; this implies that force arches developed around the dissolving particles. A 2D cross-correlation analysis between the image of large voids (Fig. 7a; Note: Grains are grown  $\Delta R/R \approx 50\%$  without displacement to close all small voids) and an image of contact force chains (Fig. 7b) confirms that most large voids were found one particle diameter away from the major force chains (and typically below; see Fig. 7c).

This distinct post-dissolution internal fabric anticipates a different sediment response upon further loading, e.g., more prone to buckling under shear perturbation. In particular, the inherent shear loading in a sloping ground may trigger static liquefaction given the high contractive tendency in soils that experienced dissolution<sup>47</sup>. This may explain the shallow slide reported in Fig. 2b.

**Displacement.** In agreement with the experimental results (Fig. 2a), vertical settlement was the prevailing global deformation pattern (Fig. S2 in the Supplemental Data). Sediments with higher soluble fractions and lower interlocking or macroscopic friction angles experienced larger amounts of settlement. Once again, vertical settlements increased quasilinearly toward the surface because of the random distribution of dissolvable grains. The third column in Table 2 shows vertical strains determined by surface settlements near the vertical walls (i.e., away from the slope). All vertical strains are well below 0.25, in agreement with increased porosity. Higher granular interlocking reduces vertical strain. In addition, vertical strains increase with the initial heights by a small degree due to gains in self-weight with increasing depth (Table 2).

The sloping ground also creates significant mass wasting, even under the fully quasi-static dissolution. As the randomly distributed soluble particles dissolve and surrounding particles are rearranged, all of the particles are mobilized vertically and horizontally (see the video—Supplementary Data). Their mobilizations are coupled during dissolution in a way that as much as particles displace vertically, horizontal movements co-occur in the sloping ground, which bears large maximum shear stresses relative to mean normal stresses (Fig. 5).

Figure 8 presents the horizontal components extracted from the final displacement vectors. Horizontal displacements were largest on the slope surface and decreased away from the slope surface without a sharp transition, that is, no shear localization. The horizontal displacements diminish gradually toward the level ground. Figure 9 quantifies the horizontal granular displacements versus the initial distance perpendicular to the slope surface in the mid slope. In all cases, horizontal grain displacement is maximum at the surface and decreases quasi-linearly with the distance from the slope surface, and becomes zero at the bottom boundaries, similar to the vertical granular displacement along the depth. It resembles simple shear flow although their movements are quasi-static.

Granular interlocking reduces horizontal displacement, and the larger initial slope angle promotes greater mass wasting (Figs. 8 and 9). Clearly horizontal displacements increase with the slope angles and decrease with

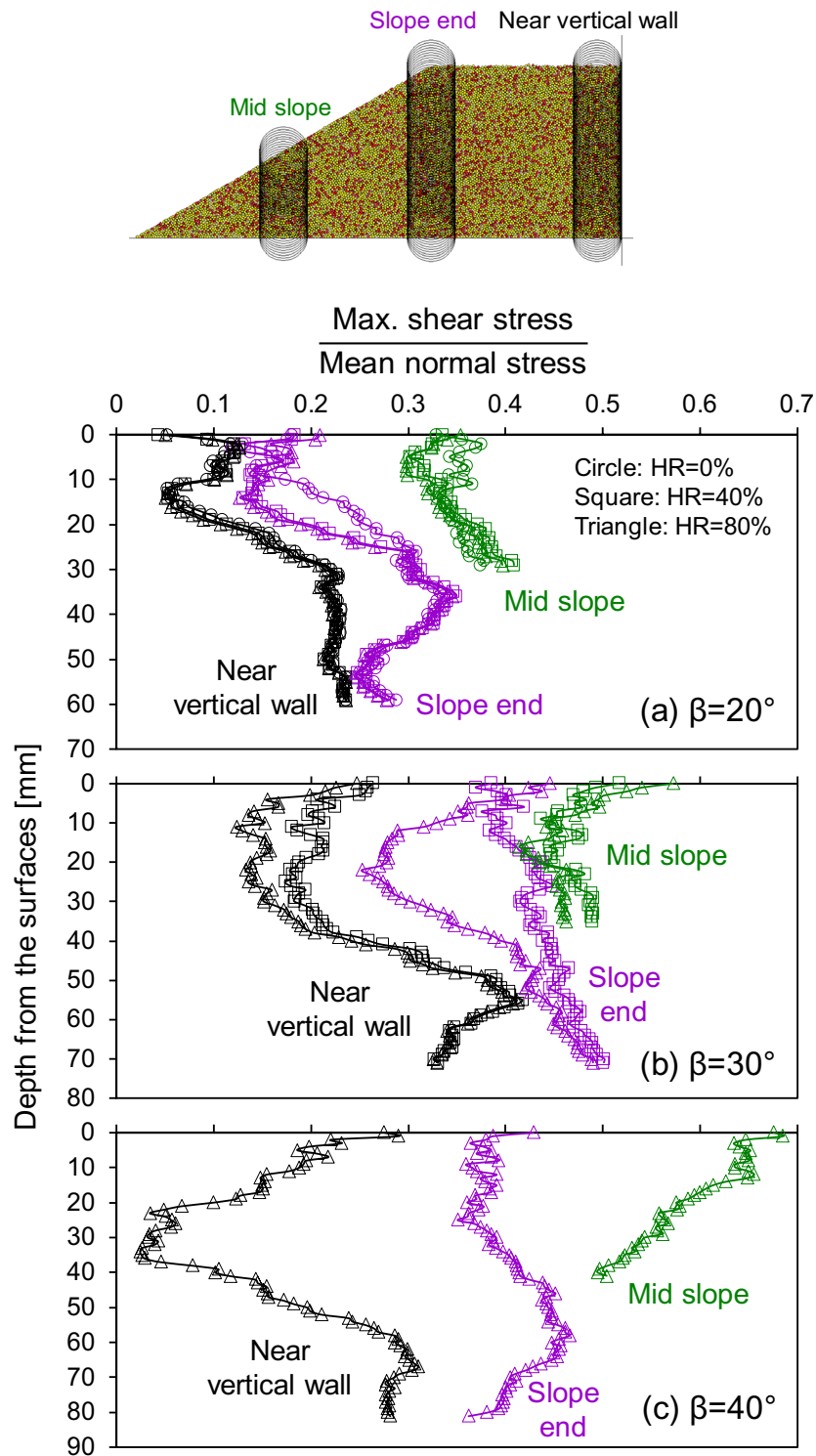


**Figure 5.** The distribution of maximum shear stress divided by the mean normal stress in the mid slopes, slope ends and near the vertical walls. Note each data point is the average value within the measurement circles located as shown.

granular interlocking more sensitively than the vertical displacements (Table 2 and Fig. 10). In addition, granular dissolution in sloping grounds increases vertical strain more than dissolution on the level ground (Table 2: compare the third and fourth columns); as grains displace horizontally, the slope geometry may create additional downward movement.



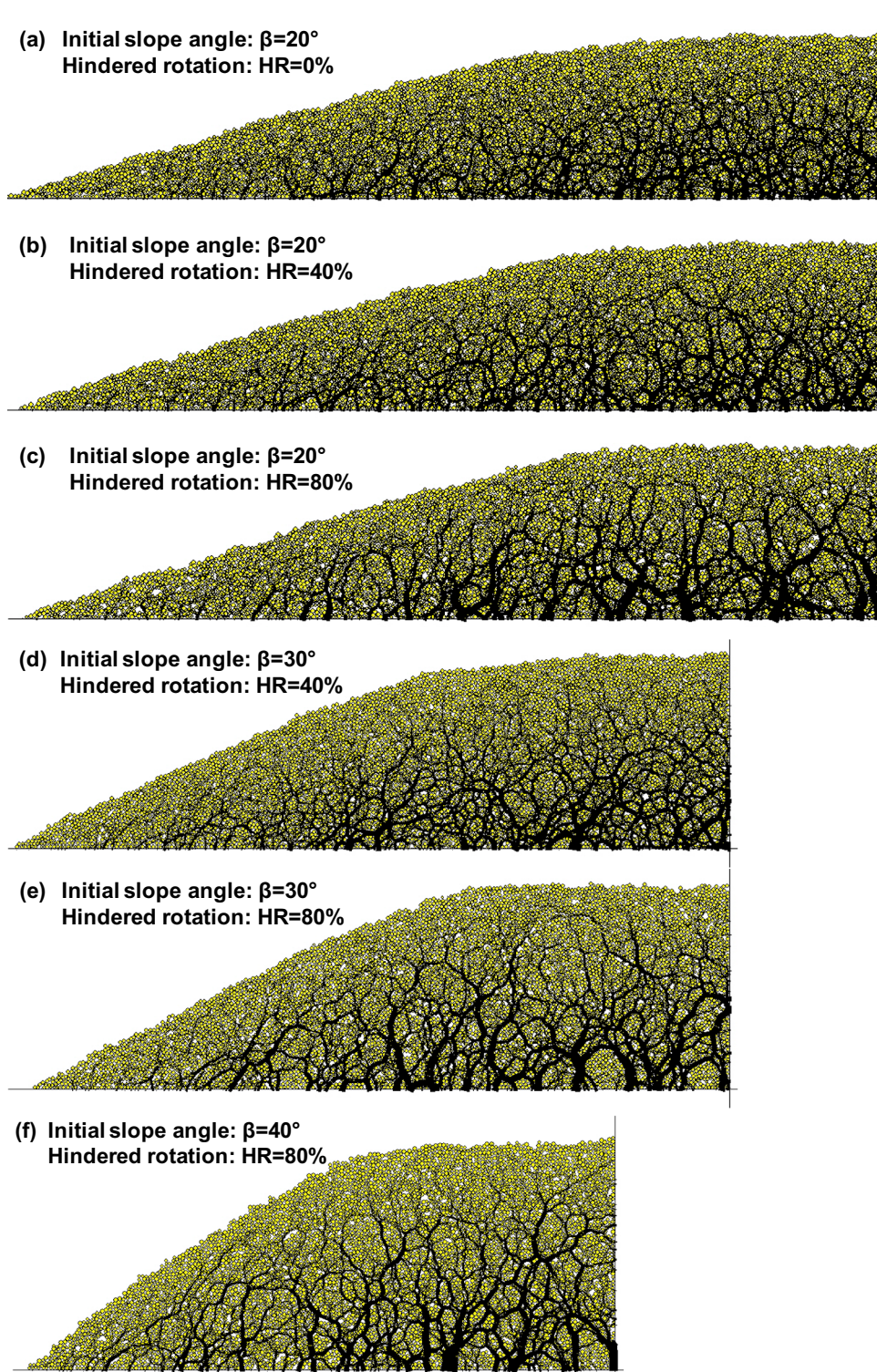
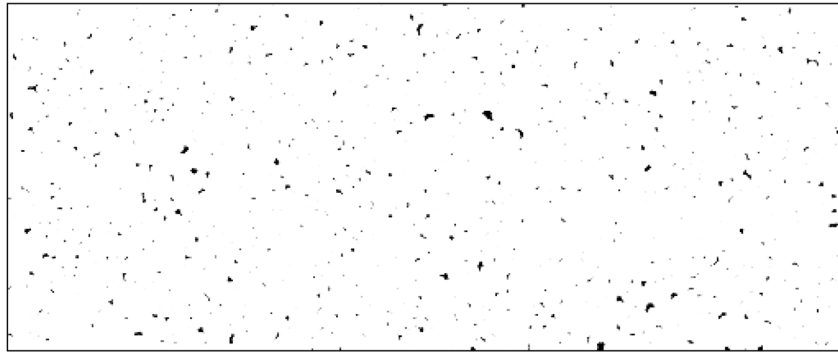


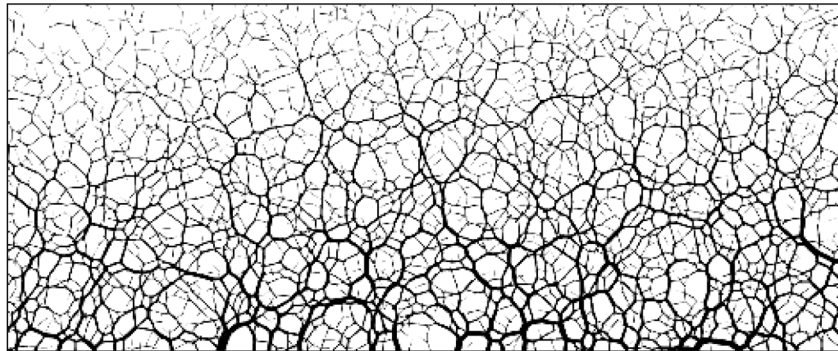
**Figure 6.** Contact force chains at the end of dissolution – All cases are shown at the same force scale. Note: Compare these results to those shown in Fig. 5.

Histograms of horizontal displacements after dissolution clearly indicate that the bulk of the medium had a mean horizontal displacement near zero (Fig. 11). The green lines show histograms for the  $\sim 2000$  particles (19% of the total number of particles) in the level ground, closest to the rigid wall on the right. In this zone, the horizontal displacements of particles are small, contained within  $\pm 2$  mm without a preferential direction; the histogram is nearly symmetric about zero displacement (Fig. 11). When all of the particles are plotted, however, significant portions are displaced horizontally outward (positive direction) (Fig. 11), which represents the grain

(a) Image of voids



(b) Image of force chains



(c) 2D image cross-correlation

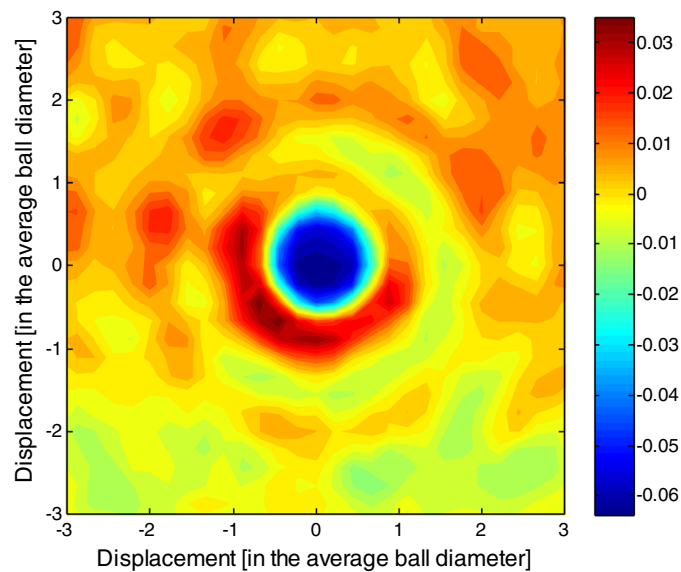


**Figure 7.** Causal link between (a) large remnant voids and (b) force chains; (c) 2D cross-correlation shows that large voids remain within a grain diameter from major force chains.

mass under the slope surface. Steeper slopes in sediments with lower granular interlocking or macroscopic friction angle showed higher horizontal displacements following dissolution, which is consistent with earlier results (Figs. 8, 9 and 10).

Initial slope angle	Hindered rotation (%)	*Vertical strain: Near vertical walls	<sup>†</sup> $\delta_v/H_0$ : Selection	<sup>‡</sup> $\delta_h/H_0$ : Selection
20°	0	0.212	0.215	0.235
	40	0.205	0.195	0.235
	80	0.163	0.130	0.065
30°	40	0.211	0.285	0.350
	80	0.176	0.175	0.122
40°	80	0.189	0.220	0.230

**Table 2.** Normalized displacements—DEM simulations. \*: Heights of level-ground portion:  $\beta_0 = 20^\circ$ : 60 mm,  $\beta_0 = 30^\circ$ : 71.2 mm,  $\beta_0 = 40^\circ$ : 82 mm. <sup>†</sup>: Vertical movements of grains at the top of the selection normalized by their initial heights. <sup>‡</sup>: Horizontal movements of grains at the top of the selection normalized by their initial heights.

## Discussions

**Field implication: mass wasting due to granular mass loss.** Certainly, the slope geometry and soluble distribution in this DEM study represent a particular case: a young sloping deposit with a limited slope extent such as energy waste or embankment that contains a soluble fraction overlies an insoluble base ground. Some field situations show that the slope surface and the lower end of the dissolution front may be parallel and the affected depth determined by the intensity and duration of each infiltration event. Rainwater infiltration may create secondary porosity in a young sloping deposit and weaken cementation in sloping sediments. In mass wasting events induced by freezing-thaw, the freezing and thawing depths are determined by the temperature difference. Layer(s) can also dominate a dissolution depth or geometry. Nevertheless, this study shows that horizontal/vertical grain movements are proportional to the affected depth of the dissolution. Also, the effects of major parameters are qualitatively recognized from this study and previous studies. While further, focused studies are required to accurately determine each effect to be useful for predicting the behavior, the following relation lends perspective to the combined effects in the absence of shear localization:

$$\delta_h, \delta_v \propto L \cdot \frac{f(\theta) \cdot g(SF) \cdot j(D)}{k(\phi)} \quad (3)$$

where each function correlates positively with the parameter inside the parentheses.  $\theta$  is the slope angle, SF the fraction of randomly distributed soluble particles,  $\phi$  the macroscopic friction angle, L the dimension of a slope, either the height or length, and D (%) the progression of dissolution that can range from 0 to ~80%, after which the movement begins to stabilize.

**Final slope angles.** The initial slope angle,  $\beta_0$ , became flatter as dissolution progressed, and the final slope was  $\beta_{final} < \beta_0$  in all cases (Fig. 12). In the absence of undrained failure, lateral displacements during dissolution had a minor effect on the slope angle; in fact, a good approximation to the final slope angle was trigonometrically computed from the shortening,  $\Delta H$ , of the initial land elevation,  $H_0$ :

$$\tan \beta_{final} = \left( 1 - \frac{\Delta H}{H_0} \right) \tan \beta_0 \quad (4)$$

Apparently, the proximity of the initial slope angle,  $\beta_0$ , to the numerically measured angle of repose,  $\beta_{repose}$ , has a secondary effect; however, granular interlocking does reduce the vertical shortening (i.e., smaller  $\Delta H/H_0$ ) and preserves steeper slopes after dissolution than less interlocked specimens, as predicted by the equation above. The soluble fraction, SF, is an upper bound estimate for vertical shortening,  $\Delta H/H_0 < SF$ —in fact,  $\Delta H/H_0 = SF$  when dissolution takes place at a constant porosity (dotted line in Fig. 12); otherwise, porosity increases during dissolution, as observed in this study.

The limited length of slope in this DEM study, as is often the case for embankments and engineered fills, creates a non-uniform slope movement. Horizontal granular displacement is more restricted near the base than on the mid slope because of the non-dissolving base material and its friction with grains of the sloping deposit. The horizontal displacement also diminishes gradually toward the level ground. Non-uniform horizontal movements thus result in slightly curved surfaces (more pronounced in high-angle slopes, e.g., Figs. 6f and 8f).

## Conclusions

Mineral dissolution and precipitation are concurrent soil processes and can take place in relatively short time scales in advective regimes and when minerals are exposed far from equilibrium, which is common in young natural and engineered systems. We investigated the effect of grain dissolution on slope stability using a 1 g model experiment complemented by discrete element simulations.

Upon dissolution, load-carrying grain arches develop around dissolving particles. A honeycomb-shaped contact force chain topology characterizes the high-porosity fabric after dissolution. The cross-correlation analysis confirms that large voids remain next to major contact force chains after dissolution. The sloping ground has high initial values of maximum shear stress relative to mean normal stress. After dissolution, the state of stress became more stable.

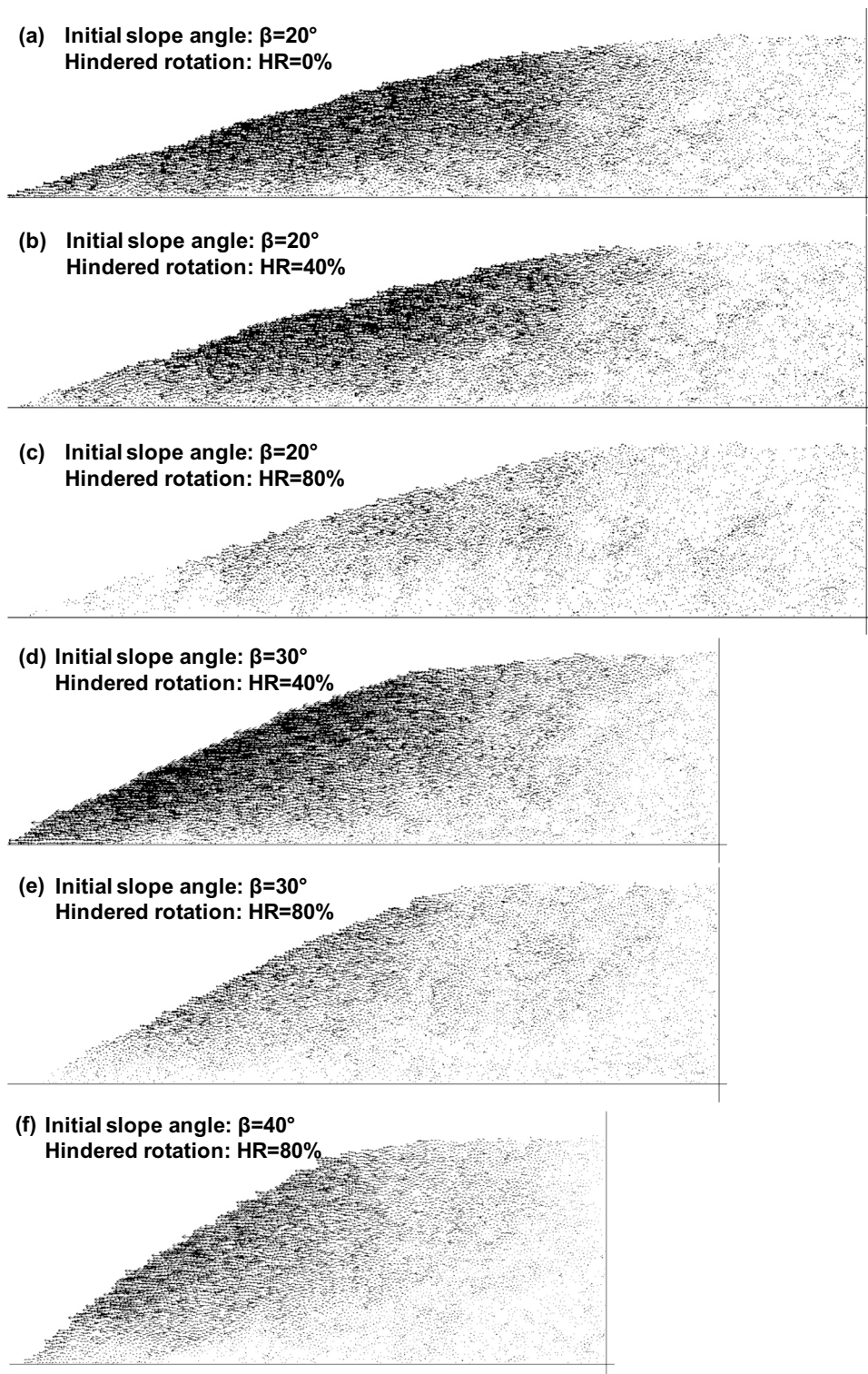


**Figure 8.** Horizontal component of the displacement vectors at the end of dissolution—All cases shown at the same displacement vector scale.

Dissolution leads to significant slope movements. While global vertical settlement is the prevailing deformation pattern, grains displace horizontally in the sloping ground, which leads to significant mass wasting even though the dissolution takes place quasi-statically. Horizontal granular movements are maximum at the slope surface and decrease linearly away from the slope surface bounded by the non-dissolving base, similar to vertical granular displacement along the depth. Sediments with a lower global friction angle or steeper slope experience larger displacements, both vertically and horizontally.

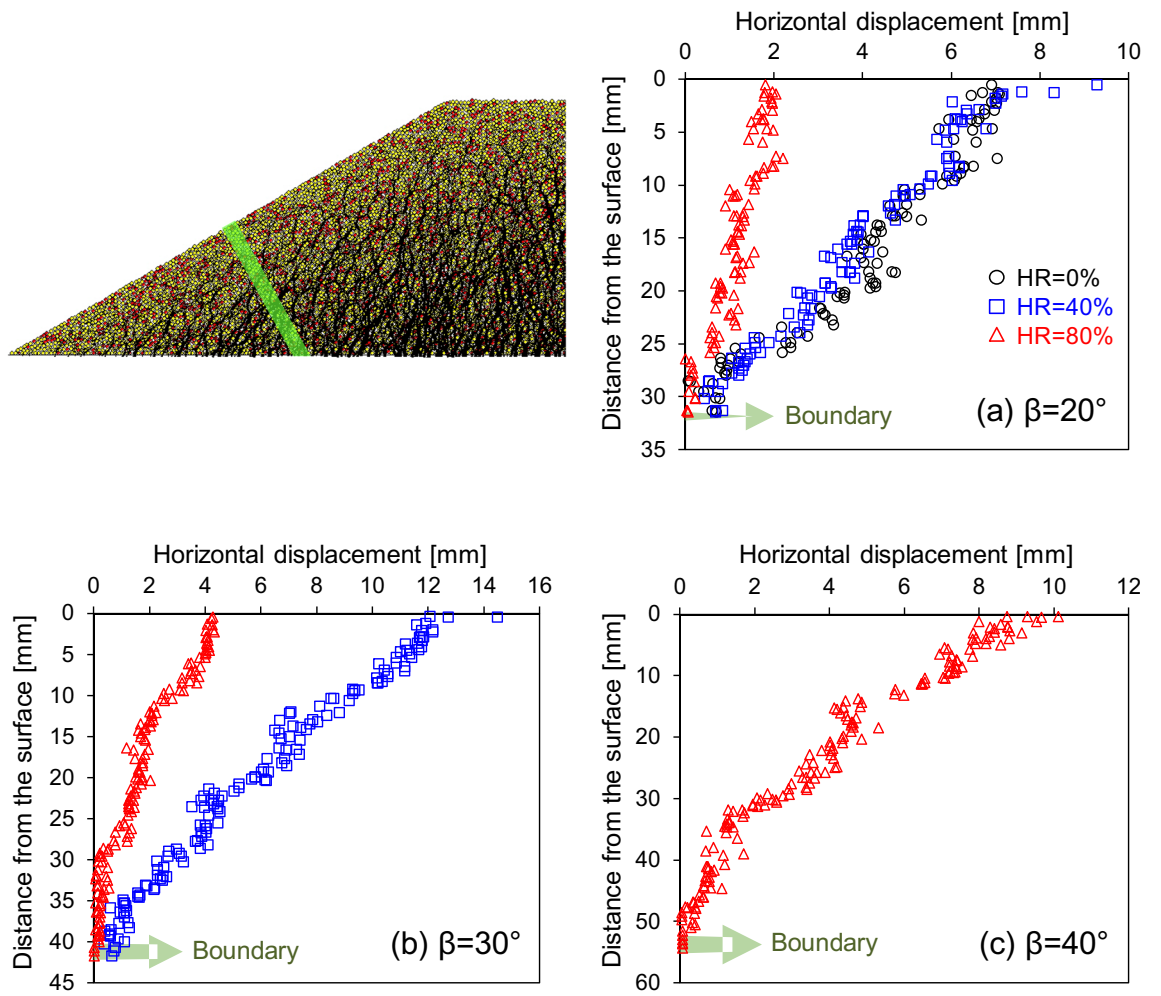


**Figure 9.** The horizontal granular displacements versus the initial distance perpendicular to the slope surface in the mid-slope. The green strip (4 mm width) shows the range of selected grains.

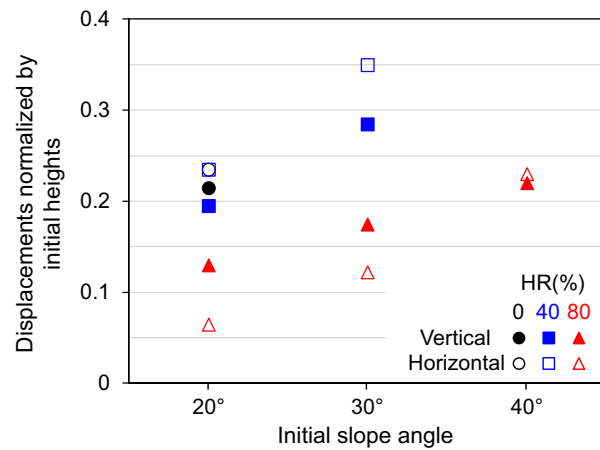


**Figure 10.** Vertical and horizontal granular displacements at the top of the selection (see Fig. 9) normalized by the initial heights from the base. Numerical data from Table 2 (the 4th and 5th columns).

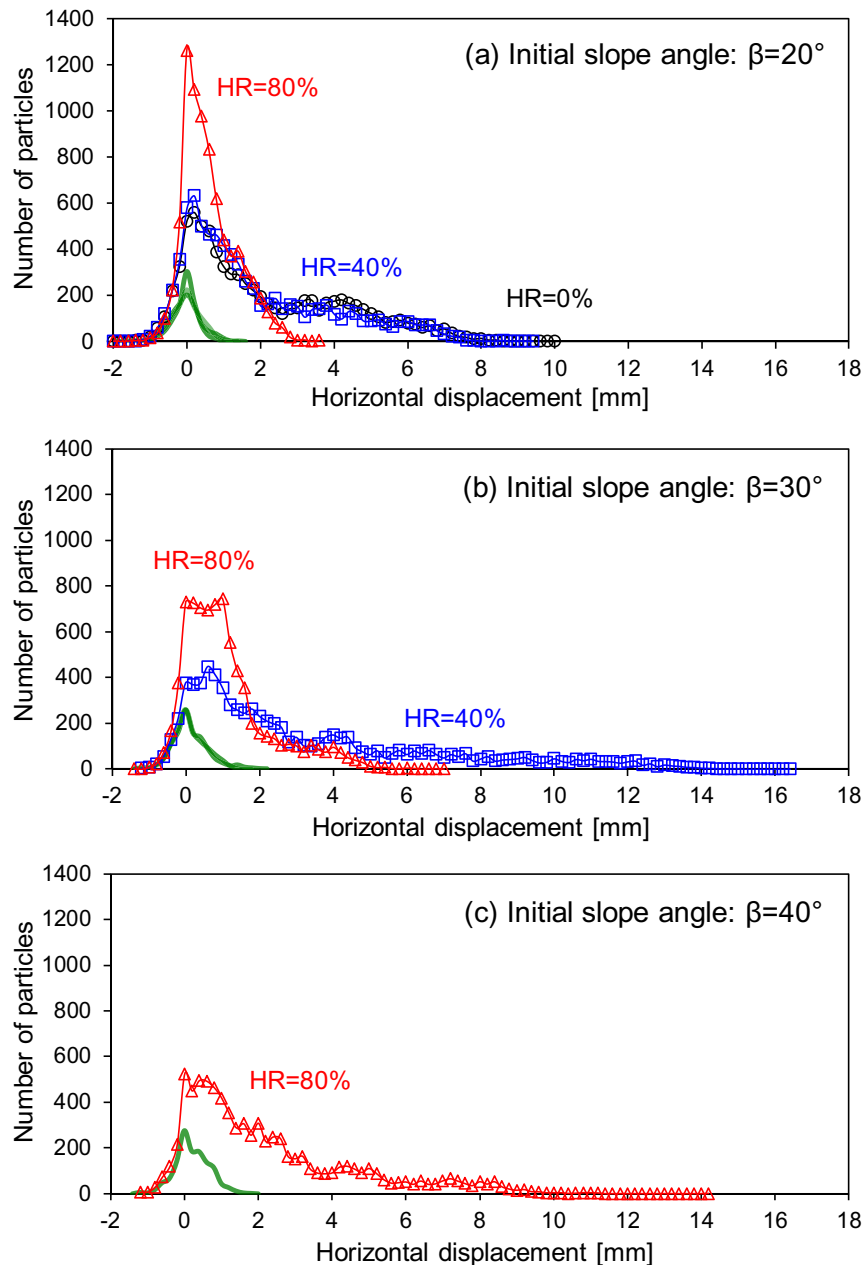


**Figure 11.** Histogram of horizontal displacements experienced by all non-dissolvable particles at the end of dissolution. Green lines show histograms for the  $\sim 2000$  particles closest to the rigid wall on the right. Bin counts are connected to facilitate visualization and distinguish among HRs (Bin size = 0.2 mm for all cases).

Slopes become flatter after dissolution; the reduction in slope angles directly related to the loss in ground elevation,  $\Delta H/H_0$ . Yet, for all cases, the slope angle is higher than the estimate from the upper bound for vertical shortening,  $\Delta H/H_0 \approx SF$ , because of increased porosities.

No shear localization or catastrophic failure was observed in the numerical simulations during dissolution under drained or dry conditions. However, sudden undrained shear may take place and lead to shallow failures. The sequence of events involves: (1) dissolution and increase in porosity, (2) internal stress approaching failure, (3) grain skeleton collapse, (4) pore pressure buildup, and (5) shear occurring as a form of static liquefaction.

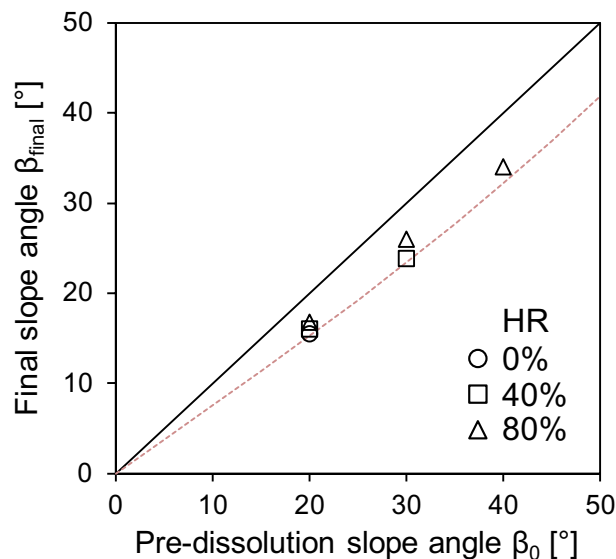


**Figure 12.** Comparison of the initial slope angle,  $\beta_0$ , and the final slope angle after dissolution,  $\beta_{\text{final}}$ , for all cases (SF = 25%). The dotted line is an upper bound estimate  $\Delta H/H_0 = SF$  when dissolution takes place at constant porosity.

### Data availability

The datasets used and/or analysed during the current study are available from the corresponding author on reasonable request.

Received: 1 September 2022; Accepted: 16 December 2022

Published online: 23 December 2022

### References

- Gutiérrez, F., Desir, G. & Gutiérrez, M. Causes of the catastrophic failure of an earth dam built on gypsiferous alluvium and dispersive clays (Altorricón, Huesca Province, NE Spain). *Environ. Geol.* **43**, 842–851. (2003).
- Herrera, M. C., Lizcano, A. & Santamarina, J. C. In *Characterization and Engineering Properties of Natural Soils* (eds T. S. Tan, K. K. Phoon, D. W. Hight, & S. Leroueil) 2385–2409 (Taylor & Francis, 2007).
- Ford, D. & Williams, P. W. *Karst Hydrogeology and Geomorphology* (Wiley, 2007).
- Stefanou, I. & Sulem, J. Chemically induced compaction bands: Triggering conditions and band thickness. *J. Geophys. Res. Solid Earth* **119**, 880–899. <https://doi.org/10.1002/2013JB010342> (2014).
- Bachus, R. C. *et al.* Characterization and engineering properties of dry and ponded class-F Fly ash. *J. Geotech. Geoenviron. Eng.* **145**, 04019003. [https://doi.org/10.1061/\(ASCE\)GT.1943-5606.0001986](https://doi.org/10.1061/(ASCE)GT.1943-5606.0001986) (2019).
- Kim, S., Espinoza, D. N., Jung, J., Cha, M. & Santamarina, J. C. in *Science of Carbon Storage In Deep Saline Formations* (eds Pania Newell & Anastasia G. Ilgen) 287–304 (Elsevier, 2019).
- Santamarina, J. C., Torres-Cruz, L. A. & Bachus, R. C. Why coal ash and tailings dam disasters occur. *Science* **364**, 526–528 (2019).
- Cha, M. & Santamarina, J. C. Hydro-chemo-mechanical coupling in sediments: Localized mineral dissolution. *Geomech. Energy Environ.* **7**, 1–9. <https://doi.org/10.1016/j.gete.2016.06.001> (2016).
- Guerrero, J., Gutiérrez, F. & Lucha, P. Paleosubsidence and active subsidence due to evaporite dissolution in the Zaragoza area (Huerva River valley, NE Spain): Processes, spatial distribution and protection measures for transport routes. *Eng. Geol.* **72**, 309–329. <https://doi.org/10.1016/j.enggeo.2003.10.002> (2004).
- Lucha, P., Cardona, F., Gutiérrez, F. & Guerrero, J. Natural and human-induced dissolution and subsidence processes in the salt outcrop of the Cardona Diapir (NE Spain). *Environ. Geol.* **53**, 1023–1035. <https://doi.org/10.1007/s00254-007-0729-3> (2008).
- Alberto, W., Giardino, M., Martinotti, G. & Tiranti, D. Geomorphological hazards related to deep dissolution phenomena in the Western Italian Alps: Distribution, assessment and interaction with human activities. *Eng. Geol.* **99**, 147–159 (2008).
- Cha, M. & Santamarina, J. C. Localized dissolution in sediments under stress. *Granular Matter* **21**, 79. <https://doi.org/10.1007/s10035-019-0932-4> (2019).
- Cha, M. & Santamarina, J. C. Volume contraction in shallow sediments: Discrete element simulation. *Appl. Sci.* **12**, 8015 (2022).
- Song, C. W., Yu, G. M. & Xue, B. F. In *2011 International Conference on Electronics, Communications and Control*. 3486–3489 (IEEE).
- Macklin, M. G. *et al.* The long term fate and environmental significance of contaminant metals released by the January and March 2000 mining tailings dam failures in Maramures County, upper Tisa Basin, Romania. *Appl. Geochem.* **18**, 241–257. [https://doi.org/10.1016/S0883-2927\(02\)00123-3](https://doi.org/10.1016/S0883-2927(02)00123-3) (2003).
- Cetin, B., Aydilek, A. H. & Li, L. Experimental and numerical analysis of metal leaching from fly ash-amended highway bases. *Waste Manag.* **32**, 965–978 (2012).
- El-Mogazi, D., Lisk, D. J. & Weinstein, L. H. A review of physical, chemical, and biological properties of fly ash and effects on agricultural ecosystems. *Sci. Total Environ.* **74**, 1–37. [https://doi.org/10.1016/0048-9697\(88\)90127-1](https://doi.org/10.1016/0048-9697(88)90127-1) (1988).
- Trivedi, A. & Sud, V. K. Collapse behavior of coal ash. *J. Geotech. Geoenviron. Eng.* **130**, 403–415. [https://doi.org/10.1061/\(asce\)1090-0241\(2004\)130:4\(403\)](https://doi.org/10.1061/(asce)1090-0241(2004)130:4(403)) (2004).
- Querol, X. *et al.* Synthesis of zeolites from coal fly ash: An overview. *Int. J. Coal Geol.* **50**, 413–423. [https://doi.org/10.1016/S0166-5162\(02\)00124-6](https://doi.org/10.1016/S0166-5162(02)00124-6) (2002).

20. Murayama, N., Yamamoto, H. & Shibata, J. Mechanism of zeolite synthesis from coal fly ash by alkali hydrothermal reaction. *Int. J. Miner. Process.* **64**, 1–17. [https://doi.org/10.1016/s0301-7516\(01\)00046-1](https://doi.org/10.1016/s0301-7516(01)00046-1) (2002).
21. Matsuoka, N. Solifluction rates, processes and landforms: A global review. *Earth Sci. Rev.* **55**, 107–134. [https://doi.org/10.1016/s0012-8252\(01\)00057-5](https://doi.org/10.1016/s0012-8252(01)00057-5) (2001).
22. Harris, C., Davies, M. C. R. & Coutard, J. P. Rates and processes of periglacial solifluction: An experimental approach. *Earth Surf. Proc. Land.* **22**, 849–868. [https://doi.org/10.1002/\(sici\)1096-9837\(199709\)22:9%3c849::aid-esp784%3e3.0.co;2-u](https://doi.org/10.1002/(sici)1096-9837(199709)22:9%3c849::aid-esp784%3e3.0.co;2-u) (1997).
23. McRoberts, E. C. & Morgenstern, N. R. The stability of thawing slopes. *Can. Geotech. J.* **11**, 447–469. <https://doi.org/10.1139/t74-052> (1974).
24. Thomas, H. R., Cleall, P. J., Li, Y., Harris, C. & Kern-Luetsch, M. Modelling of cryogenic processes in permafrost and seasonally frozen soils. *Geotechnique* **59**, 173–184 (2009).
25. Skempton, A. W. & Vaughan, P. R. The failure of Carsington dam. *Geotechnique* **43**, 151–173 (1993).
26. Potts, D. M., Dounias, G. T. & Vaughan, P. R. Finite-element analysis of progressive failure of Carsington embankment. *Geotechnique* **40**, 79–101 (1990).
27. Dramis, F., Govi, M., Guglielmin, M. & Mortara, G. Mountain permafrost and slope instability in the Italian Alps: The Val Pola Landslide. *Permafrost Periglac. Process.* **6**, 73–81. <https://doi.org/10.1002/ppp.3430060108> (1995).
28. Darrow, M. M., Gyswy, N. L., Simpson, J. M., Daanen, R. P. & Hubbard, T. D. Frozen debris lobe morphology and movement: An overview of eight dynamic features, southern Brooks Range, Alaska. *Cryosphere* **10**, 977–993 (2016).
29. Wei, M., Fujun, N., Satoshi, A. & Dewu, J. Slope instability phenomena in permafrost regions of Qinghai-Tibet Plateau, China. *Landslides* **3**, 260–264. <https://doi.org/10.1007/s10346-006-0045-0> (2006).
30. Higman, B. *et al.* The 2015 landslide and tsunami in Taan Fiord, Alaska. *Scientific Rep.* **8**, 12993. <https://doi.org/10.1038/s41598-018-30475-w> (2018).
31. Gruber, S. & Haeblerli, W. Permafrost in steep bedrock slopes and its temperature-related destabilization following climate change. *J. Geophys. Res. Earth Surf.* **112** (2007).
32. Huggel, C. *et al.* Ice thawing, mountains falling—are alpine rock slope failures increasing?. *Geol. Today* **28**, 98–104. <https://doi.org/10.1111/j.1365-2451.2012.00836.x> (2012).
33. Sultan, N., Cochonat, P., Foucher, J. P. & Mienert, J. Effect of gas hydrates melting on seafloor slope instability. *Mar. Geol.* **213**, 379–401 (2004).
34. Nixon, M. F. & Grozic, J. L. H. Submarine slope failure due to gas hydrate dissociation: A preliminary quantification. *Can. Geotech. J.* **44**, 314–325. <https://doi.org/10.1139/t06-121> (2007).
35. Geissler, W. H. *et al.* Arctic megaslide at presumed rest. *Sci. Rep.* **6**, 38529. <https://doi.org/10.1038/srep38529> (2016).
36. Elger, J. *et al.* Submarine slope failures due to pipe structure formation. *Nat. Commun.* **9**, 715. <https://doi.org/10.1038/s41467-018-03176-1> (2018).
37. Sawyer, D. E., Mason, R. A., Cook, A. E. & Portnov, A. Submarine landslides induce massive waves in subsea Brine pools. *Sci. Rep.* **9**, 128. <https://doi.org/10.1038/s41598-018-36781-7> (2019).
38. Bugge, T., Belderson, R. H. & Kenyon, N. H. The storegga slide. *Phil Transactions R Soc Lond Ser Math Phys Eng Sci* **325**, 357–388. <https://doi.org/10.1098/rsta.1988.0055> (1988).
39. Bourriak, S., Vanneste, M. & Saoutkine, A. Inferred gas hydrates and clay diapirs near the Storegga Slide on the southern edge of the Voring Plateau, offshore Norway. *Mar. Geol.* **163**, 125–148. [https://doi.org/10.1016/s0025-3227\(99\)00115-2](https://doi.org/10.1016/s0025-3227(99)00115-2) (2000).
40. Laberg, J. S. & Vorren, T. O. The Traenadjupet Slide, offshore Norway—morphology, evacuation and triggering mechanisms. *Mar. Geol.* **171**, 95–114. [https://doi.org/10.1016/s0025-3227\(00\)00112-2](https://doi.org/10.1016/s0025-3227(00)00112-2) (2000).
41. Sultan, N. *et al.* Triggering mechanisms of slope instability processes and sediment failures on continental margins: A geotechnical approach. *Mar. Geol.* **213**, 291–321. <https://doi.org/10.1016/j.margeo.2004.10.011> (2004).
42. Kwon, T. H., Cho, G. C. & Santamarina, J. C. Gas hydrate dissociation in sediments: Pressure-temperature evolution. *Geochem. Geophys. Geosyst.* **9**, 1–14. <https://doi.org/10.1029/2007gc001920> (2008).
43. Maslin, M., Vilela, C., Mikkelsen, N. & Grootes, P. Causes of catastrophic sediment failures of the Amazon fan. *Quatern. Sci. Rev.* **24**, 2180–2193. <https://doi.org/10.1016/j.quascirev.2005.01.016> (2005).
44. Kvenvolden, K. A. Gas hydrates - geological perspective and global change. *Rev. Geophys.* **31**, 173–187 (1993).
45. Kvenvolden, K. A. Gas hydrate and humans. *Ann. N. Y. Acad. Sci.* **912**, 17–22. <https://doi.org/10.1111/j.1749-6632.2000.tb06755.x> (2000).
46. Vanoudheusden, E., Sultan, N. & Cochonat, P. Mechanical behaviour of unsaturated marine sediments: Experimental and theoretical approaches. *Mar. Geol.* **213**, 323–342. <https://doi.org/10.1016/j.margeo.2004.10.012> (2004).
47. Cha, M. & Santamarina, J. C. Dissolution of randomly distributed soluble grains: Post dissolution  $k_0$ -loading and shear. *Géotechnique* **64**, 828–836. <https://doi.org/10.1680/geot.14.P.115> (2014).
48. MiDi, G. D. R. On dense granular flows. *Eur. Phys. J. E* **14**, 341–365 (2004).
49. Saingier, G., Deboeuf, S. & Lagrée, P.-Y. On the front shape of an inertial granular flow down a rough incline. *Phys. Fluids* **28**, 053302 (2016).
50. Shin, H. & Santamarina, J. C. Mineral dissolution and the evolution of  $k_0$ . *J. Geotech. Geoenviron. Eng.* **135**, 1141–1147 (2009).
51. Weisbrod, N., Dahan, O. & Adar, E. M. Particle transport in unsaturated fractured chalk under arid conditions. *J. Contam. Hydrol.* **56**, 117–136. [https://doi.org/10.1016/S0169-7722\(01\)00199-1](https://doi.org/10.1016/S0169-7722(01)00199-1) (2002).
52. Gordon, S. J. & Brady, P. V. In situ determination of long-term basaltic glass dissolution in the unsaturated zone. *Chem. Geol.* **190**, 113–122. [https://doi.org/10.1016/S0009-2541\(02\)00113-4](https://doi.org/10.1016/S0009-2541(02)00113-4) (2002).
53. Itasca Consulting Group. (Itasca Consulting Group Inc Minnesota, 2004).
54. McDowell, G., Li, H. & Lowndes, I. The importance of particle shape in discrete-element modelling of particle flow in a chute. *Géotechnique Lett.* **1**, 59–64 (2011).
55. Wang, G., Zhang, W., Ji, M., Miao, H. & Jin, Z. Numerical simulation and parameter optimization of earth auger in hilly area using EDEM software. *Sci. Rep.* **12**, 1–14 (2022).
56. Makange, N. R., Ji, C., Nyalala, I., Sunusi, I. I. & Opiyo, S. Prediction of precise subsoiling based on analytical method, discrete element simulation and experimental data from soil bin. *Sci. Rep.* **11**, 1–12 (2021).
57. Mohamed, A. & Gutierrez, M. Comprehensive study of the effects of rolling resistance on the stress-strain and strain localization behavior of granular materials. *Granular Matter* **12**, 527–541. <https://doi.org/10.1007/s10035-010-0211-x> (2010).
58. Fukumoto, Y., Sakaguchi, H. & Murakami, A. The role of rolling friction in granular packing. *Granular Matter* **15**, 175–182 (2013).
59. Iwashita, K. & Oda, M. Rolling resistance at contacts in simulation of shear band development by DEM. *J. Eng. Mech. Asce.* **124**, 285–292 (1998).
60. Jiang, M., Shen, Z. & Wang, J. A novel three-dimensional contact model for granulates incorporating rolling and twisting resistances. *Comput. Geotech.* **65**, 147–163. <https://doi.org/10.1016/j.compgeo.2014.12.011> (2015).
61. Lu, M. & McDowell, G. The importance of modelling ballast particle shape in the discrete element method. *Granular Matter* **9**, 69–80 (2007).
62. Guises, R., Xiang, J., Latham, J.-P. & Munjiza, A. Granular packing: Numerical simulation and the characterisation of the effect of particle shape. *Granular Matter* **11**, 281–292 (2009).
63. Wu, M., Wang, J., Russell, A. & DEM Cheng, Z. modelling of mini-triaxial test based on one-to-one mapping of sand particles. *Géotechnique* **71**, 714–727. <https://doi.org/10.1680/jgeot.19.P.212> (2021).



64. Wu, M., Wang, J. & DEM Zhao, B. modeling of one-dimensional compression of sands incorporating statistical particle fragmentation scheme. *Can. Geotech. J.* **59**, 144–157 (2022).
65. Bardet, J. P. Observations on the effects of particle rotations on the failure of idealized granular materials. *Mech. Mater.* **18**, 159–182 (1994).
66. Suiker, A. S. J. & Fleck, N. A. Frictional collapse of granular assemblies. *J. Appl. Mech.* **71**, 350–358 (2004).
67. Cha, M. & Santamarina, J. C. Effect of dissolution on the load-settlement behavior of shallow foundations. *Can. Geotech. J.* **53**, 1353–1357 (2016).
68. Bui, E. N., Loeppert, R. H. & Wilding, L. P. Carbonate phases in calcareous soils of the Western United States. *Soil Sci. Soc. Am. J.* **54**, 39–45. <https://doi.org/10.2136/sssaj1990.03615995005400010006x> (1990).
69. Washbourne, C.-L., Lopez-Capel, E., Renforth, P., Ascough, P. L. & Manning, D. A. Rapid removal of atmospheric CO<sub>2</sub> by urban soils. *Environ. Sci. Technol.* **49**, 5434–5440 (2015).
70. Tran, M. K., Shin, H., Byun, Y.-H. & Lee, J.-S. Mineral dissolution effects on mechanical strength. *Eng. Geol.* **125**, 26–34. <https://doi.org/10.1016/j.enggeo.2011.10.014> (2012).
71. Shin, H., Santamarina, J. C. & Cartwright, J. A. Contraction-driven shear failure in compacting uncemented sediments. *Geology* **36**, 931–934. <https://doi.org/10.1130/g24951a.1> (2008).
72. da Cruz, F., Emam, S., Prochnow, M., Roux, J.-N. & Chevoir, F. Rheophysics of dense granular materials: Discrete simulation of plane shear flows. *Phys. Rev. E* **72**, 021309 (2005).
73. Cha, M. & Santamarina, J. C. Predissolution and postdissolution penetration resistance. *J. Geotech. Geoenviron. Eng.* **139**, 2193–2200. [https://doi.org/10.1061/\(asce\)gt.1943-5606.0000949](https://doi.org/10.1061/(asce)gt.1943-5606.0000949) (2013).

## Acknowledgements

Support for this research was provided by the KAUST endowment and the US Department of Energy Savannah River Operations Office. This research was also supported by Basic Science Research Program through the National Research Foundation of Korea (NRF) funded by the Ministry of Education (2019R1A6A1A10072987). G. Abelskamp edited the manuscript.

## Author contributions

J.C.S. conceptualized and supervised the investigation. M.C. performed numerical and experimental works. M.C. drafted the manuscript. J.C.S. edited the manuscript. All authors reviewed the manuscript.

## Competing interests

The authors declare no competing interests.

## Additional information

**Supplementary Information** The online version contains supplementary material available at <https://doi.org/10.1038/s41598-022-26620-1>.

**Correspondence** and requests for materials should be addressed to M.C.

**Reprints and permissions information** is available at [www.nature.com/reprints](http://www.nature.com/reprints).

**Publisher's note** Springer Nature remains neutral with regard to jurisdictional claims in published maps and institutional affiliations.



**Open Access** This article is licensed under a Creative Commons Attribution 4.0 International License, which permits use, sharing, adaptation, distribution and reproduction in any medium or format, as long as you give appropriate credit to the original author(s) and the source, provide a link to the Creative Commons licence, and indicate if changes were made. The images or other third party material in this article are included in the article's Creative Commons licence, unless indicated otherwise in a credit line to the material. If material is not included in the article's Creative Commons licence and your intended use is not permitted by statutory regulation or exceeds the permitted use, you will need to obtain permission directly from the copyright holder. To view a copy of this licence, visit <http://creativecommons.org/licenses/by/4.0/>.

© The Author(s) 2022